Spontaneous polarization in ultrasmall lithium niobate nanocrystals revealed by second harmonic generation

Bastian Knabe* and Karsten Buse

Department of Microsystems Engineering (IMTEK), University of Freiburg Georges-Köhler-Allee 102, 79110 Freiburg, and Fraunhofer Institute for Physical Measurement Techniques Heidenhofstraße 8, 79110 Freiburg, Germany

Wilfried Assenmacher and Werner Mader

Institute of Inorganic Chemistry, University of Bonn, Römerstraße 164, 53117 Bonn, Germany

(Received 8 May 2012; revised manuscript received 6 September 2012; published 26 November 2012)

Nanocrystals of lithium niobate ($LiNbO_3$) with diameters of between 5 and 50 nm were produced by a combination of sol-gel synthesis and wet-chemical etching. The phase purity and nearly spherical shape of the crystals were verified by transmission electron microscopy. Power and polarization dependences of the second harmonic signal of single nanocrystals reveal that the nanocrystals have the noncentrosymmetric point group $3m$ and that the second-order nonlinear optical coefficients known from the bulk material are fully present in all nanocrystals studied. The volume of the crystals is still the main source of frequency conversion and they are spontaneously polarized.

DOI: 10.1103/PhysRevB.86.195428 PACS number(s): 78.67.Bf, 77.84.Ek, 42.65.Ky, 81.07.Bc

I. INTRODUCTION

Noncentrosymmetric crystals exhibit many relevant symmetry-induced properties, such as second-order optical nonlinearities and piezoelectric effects. Examples of such materials are lithium niobate ($LiNbO_3$) and barium titanate ($BaTiO_3$). Most of the knowledge available on these materials has been gained from studies of bulk crystals. There are plenty of indications that the material properties may change if the material is of nanoscopic size.

As an extreme impact, a switch to a centrosymmetric structure is predicted, e.g., for perovskites.[1,2] Experimental studies on $BaTiO_3$ provide so far an inconclusive picture: Size thresholds for a paraelectric-ferroelectric phase transition between less than 10 and 120 nm have been reported.[3–8] For $LiNbO_3$ only a few attempts have been made to elucidate whether there are size-dependent properties of nanoscopic samples, both theoretically and experimentally.[9–11]

In this work we utilize the nonlinear optical (NLO) response of $LiNbO_3$ nanocrystals as a probe for the structural symmetry. Besides gaining a deeper physical understanding, the work is also of practical relevance: Crystalline NLO materials are important as they enable diverse applications in the field of photonics, e.g., second harmonic (SH) generation for conversion of infrared into visible light and optical parametrical oscillation or amplification for generation of highly tunable coherent light. For these three-wave-mixing applications, $LiNbO_3$ is one of the widely used NLO materials.[12]

Quite recently nanometer-sized NLO materials have received interest, as they could enable the building of coherent subwavelength light sources.[13–17] Even more applications are conceivable, e.g., their use as nonresonant markers in SH generation microscopy, with the advantage of coherently generated light and robustness against bleaching, contrary to dyes, and no blinking plus a flat frequency conversion response, contrary to quantum dots.[15,18] Moreover, one can transfer the beneficial properties of small NLO crystals to hybrid materials by embedding them into easily processable polymers.[19]

To achieve all these goals we fabricate $LiNbO_3$ nanocrystals through cascading a bottom-up sol-gel method, with a top-down etching method. Power- and polarization-dependent SH generation experiments with single nanocrystals are performed. These measurements reveal, through a theoretical analysis, full information about their NLO response.[20]

II. SAMPLE PREPARATION

Size reduction by etching has the benefit that the fundamental material is the same for all samples, i.e., that varying crystal growth parameters are not an issue. Having the diameters of the crystals already on the nanometer scale after the first fabrication step minimizes the effort required for the second step and hence the volume loss.

We use a bottom-up alkoxide sol-gel method for crystal fabrication and achieve the final crystal size by applying a subsequent top-down method consisting of wet-chemical etching using hydrofluoric acid (HF). The bottom-up synthesis and crystallization of the crystals are described elsewhere in detail.[10,21] Here we present a general description of the etching procedure. For the complete description we refer to the Supplementary Material, which is available online.[22] The single crystals were suspended in ethanol. This dispersion is called as grown (AG) and is the starting material, as well as the reference, for subsequent processing.

For every batch, HF was added to the suspension to yield 2.6% HF, 5.0% HF, and 9.2% HF concentrations, or 95, 180, and 335 mM, respectively. The samples were etched for 5 to 30 min. Table I gives an overview of all etched batches and their names used within this article.

For electron microscopy, the samples were prepared on holey carbon films, supported by copper grids, from the ethanol suspension. For NLO characterization the batches were further diluted by adding ethanol and prepared on glass slides by slow evaporation of a suspension drop on the substrate. The particle concentration in the suspension was adjusted to yield a final density on the glass substrate of not more than roughly one

 ©2012 American Physical Society

TABLE I. Prepared samples, with the abbreviations used.

Etch time (min)	2.6% HF (95 mM)	5.0% HF (180 mM)	9.2% HF (335 mM)
0	AG	AG	AG
5	—	M5	—
10	—	M10	H10
15	L15	—	—
20	—	M20	H20
30	L30	M30	—

crystal per 10 μm^2. The crystals were finally placed directly on the glass substrate and fixated by surface adhesion. A possible angular correlation for the deposited single crystals could be ruled out, since it was shown that the electrical fields needed for a significant individual orientation, while in suspension, have to be of considerable strength, $\approx$1 V/μm.[23]

III. METHODS FOR SECOND HARMONIC CHARACTERIZATION

A. Experimental setup

Figure 1 shows schematically the setup used for NLO characterization. The core of the setup consists of two microscope objectives, with a 40× magnification, 0.65-numerical-aperture (NA) objective for focusing, and a 100× magnification, 1.45-NA oil-immersion objective for light collection, in confocal geometry. The crystals are not immersed in the index matching oil. The pump wave is supplied by a laser emitting linearly polarized 1064-nm-wavelength, 1.0-ns pulses with a nearly Gaussian beam profile. The upper objective focuses the pump beam to a $w_0 = 1.0$ μm waist.

We always provide the SH pulse energy, averaged for several pump pulses, that is detected. For further details we refer to the Supplementary Material, which is available online and describes, in particular, the procedure to ensure that only single crystals are present in the center of the pump focus.[22]

Single crystals were examined for their polarization-dependent SH response at an $I = 80$ GW/cm^2 pump intensity.

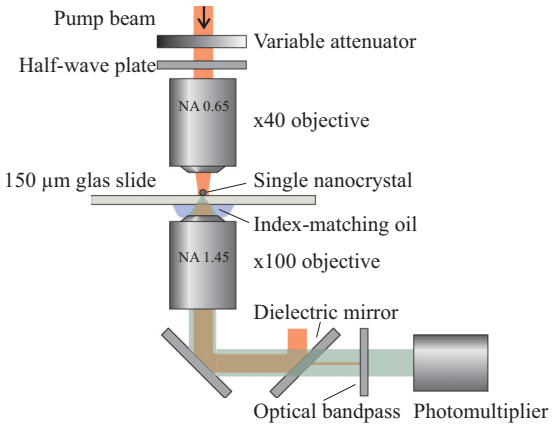

FIG. 1. (Color online) Experimental setup for second harmonic measurements. The laser delivers linearly polarized 1.0-ns pulses at a 1064-nm wavelength. The polarization direction in the focal plane can be adjusted using a rotatable half-wave plate.

TABLE II. Transmissivities and detection efficiencies of components used.

	Optical part	Power reduction factor
Pump side		
at 1064 nm	40× objective	0.77
Detection side		
at 532 nm	100× objective	0.88
	Collection efficiency (see Sec. III B)	0.81
	Filter array	0.78
	PMT quantum efficiency	0.35

Also, selected pump-intensity-dependent SH response curves were measured at maximum or minimum conversion polarizations.

The SH light generated by the glass substrate was measured and subtracted for all measurements. Although the background was very constant through all experiments, we defined the background level as the signal threshold a crystal has to have to be included for statistics. The highest measured signal was roughly 10^5 times stronger than the background.

For specifying the pump power that is present at the crystal, the transmittance of the objective is considered as a reduction coefficient. Table II summarizes all loss factors that are considered for calculation of the total emission of the nanocrystals.

B. Theoretical considerations

1. *Second harmonic generation*

We want to provide an expression for describing the power of the SH wave emitted by a single, randomly oriented, and spherical $LiNbO_3$ nanocrystal, which is pumped by a focused infrared light wave. Even more, we want to provide an expression which enables us to determine, from the measured power of the emitted SH wave, the nonlinear coefficient of a single nanocrystal in the focal spot.

If this nanocrystal with diameter L is much smaller than the crystal internal wavelengths of the participating light waves, one can treat the light as a time-varying, but spatially homogeneous electrical field. This is called the "quasielectrostatic approximation," which treats the nanocrystal like a point dipole antenna.[24] Considering this, the amplitude of the crystal internal electrical field E of a plane pump wave is given by[24]

$$E = \frac{3n_h^2}{2n_h^2 + n_1^2} f \sqrt{\frac{2n_1 I}{c_0 \epsilon_0}}, \tag{1}$$

$$\text{with} \quad I = 2P_1 / \left(\pi w_0^2\right), \tag{2}$$

where n_1 is the refractive index for light of the pump wave; n_h, that of the surrounding medium, here air; f is a reduction factor; I is the peak intensity of the Gaussian pump beam; c_0 is the vacuum speed of light; ϵ_0 is the vacuum permittivity; P_1 is the pump power; and w_0 is the beam waist radius. For the sake of brevity, we assume an isotropic refractive index for the nanocrystals, being the weighted average of the ordinary and extraordinary refractive indices for light of the pump wave,

$n_o = 2.232$ and $n_e = 2.156$, respectively.[25] This assumption gives an isotropic approximation for the determination of the electrical field within the crystal. The accuracy of this conventional isotropic approximation is, rigorously speaking, unknown.

Furthermore, we have to consider that the nanocrystals are in the node of a standing wave arising from interference of the pump wave and its substrate-reflected counterpropagating part. This modulation of the pump intensity is relevant, since the nanocrystals are too small to average across the standing wave. Therefore, the reduction factor $f \approx 0.8$ has been introduced.

This strong electric field gives rise to a polarization of the crystal, which can be described tensorially as $\mathcal{P}_i = \epsilon_0 \chi^{(1)}_{ij} E_j + 2\epsilon_0 d_{ijk} E_j E_k + \ldots$, where the second term is the well-known nonlinear polarization $\mathcal{P}^{(2)}$, enabling three-wave mixing. The nonzero components of d for $LiNbO_3$ are $d_{33} = -27$ pm/V, $d_{22} = -3.2$ pm/V, and $d_{31} = d_{15} = -4.7$ pm/V at a pump wavelength of 1 μm in contracted matrix notation.[26]

When only the second-order part of the polarization is considered, the crystal exhibits dipole moments oscillating at a frequency that is twice the pump-wave frequency. The total emitted light power from the nanocrystals acting like oscillating point dipoles can be approximated with[27]

$$W_2 = \frac{c_0^2 Z_0 k_2^4 V^2}{12\pi} \sum_i \left(\mathcal{P}_i^{(2)}\right)^2, \tag{3}$$

when the crystal is pumped with a monochromatic wave, where Z_0 is the vacuum impedance, k_2 is the wave vector of the SH, and $V = (4/3)\pi(L/2)^3$ is the volume of the spherical nanocrystal. Since $\sum_i (\mathcal{P}_i^{(2)})^2 \propto I^2$, Eq. (3) exhibits the usual quadratic dependence of the SH power on the pump intensity. But because $W_2 \propto V^2$ it shows a dependence of the SH power on the crystal size L to the power of 6, similarly to that of linear Rayleigh scattering. With separation into the three elementary dipole moments, Eq. (3) yields

$$W_2 = \frac{k_2^4 V^2}{3\pi Z_0} \sum_i (d_{ijk} E_j E_k)^2. \tag{4}$$

With Eq. (4) it is straightforward to determine the radiated power with the known tensor components of $LiNbO_3$, but here the inverse problem is faced: An SH response is measured from a nanocrystal with an unknown orientation. If the response is measured independently of the output polarization, the sum in Eq. (4) collapses to the effective $d_m^2(\xi)$,

$$W_2(\xi) = \frac{k_2^4 V^2}{3\pi Z_0} d_m^2(\xi) E^4. \tag{5}$$

With the rotation of the pump-wave polarization by the angle ξ, e.g., using a half-wave plate, the response can be probed for a single rotation axis. But this degree of freedom is hardly sufficient for a complete analysis of the nonlinear coefficients. The complete crystal orientation, involving two more angles ϕ and θ, where ϕ is the zenith angle and θ the azimuth angle of the crystal, in the laboratory coordinate system has to be considered to predict a theoretical $d_m^2(\xi)$. Thus two tasks have to be completed. First, the effective $d_m^2(\xi)$ has to be predicted for an arbitrary crystal orientation from the bulk crystal tensor components. Second, clearly discernible patterns of the responses have to be found in the predictions, where the d_m^2 ideally has an invariant value, regardless of individual crystal orientation. The second part is important since the size distribution, as well as the arbitrary orientation, of the samples leads to a response distribution as well.

2. *Orientation issues*

To contract the tensorial expression into a scalar one, we use an approach similar to that of Hsieh *et al.*:[18,28] The arbitrary crystal orientation is modeled by applying a Euler transformation matrix in *ZYX* notation $\hat{U}(\theta,\phi,\psi)$ to the vector of the electrical field of the pump beam in the laboratory coordinate system. We define $\vec{E} = E\,\vec{e}_z$ and we use the matrix form, instead of the tensorial one, for the sake of brevity. Using $\hat{U}(\theta,\phi,\psi)$, the angle ψ represents the input light polarization angle, e.g., determined by a half-wave plate in the pump beam. Rotations by ϕ and θ turn this light polarization into the crystal reference frame.

The nonlinear polarization then reads

$$\vec{d}_m(\theta,\phi,\psi) = \hat{d}(\hat{U}(\theta,\phi,\psi)\vec{e}_z), \tag{6}$$

$$\vec{\mathcal{P}}^{(2)} = 2\epsilon_0\, \vec{d}_m(\theta,\phi,\psi)\, E^2. \tag{7}$$

Therefore $|\vec{d}_m(\theta,\phi,\psi)|$ gives the effective total scalar nonlinear coefficient $d_m(\theta,\phi,\psi)$. Figure 2 shows curves for $d_m(\theta,\phi,\psi)$ with varied ψ for certain sets of θ and ϕ.

Two points are always distinguishable in these patterns, the minimum and the maximum. The minimum is always reached when the light polarization lies in the plane defined by the a axes of the $LiNbO_3$ crystal. For all values of θ and ϕ, a value of ψ can be found to achieve that. The value of minimum is calculated according to

$$d_m^{\min} = \sqrt{d_{22}^2 + d_{31}^2} = 5.6 \text{ pm/V}, \tag{8}$$

when assuming the NLO coefficients of bulk crystals. The minimum SH response of every single crystal in the experiments can be calculated by this effective NLO coefficient.

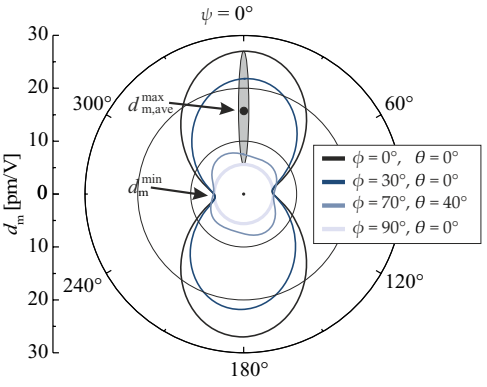

FIG. 2. (Color online) Polar plot of the calculated scalar $d_m(\theta,\phi,\psi)$ for certain sets of θ and ϕ. The angle ψ is varied. A light polarization perpendicular to the crystal c axis corresponds to $\phi = 90°$, while $\psi = \phi = 0°$ corresponds to a light polarization parallel to the c axis. Note that the minimum value for each curve is always the same $d_m^{\min}$, while the maximum varies between 27 and 5.6 pm/V. The average maximum is calculated via Eq. (9).

In contrast to the minimum, which always stays at 5.6 pm/V, the range of possible maximum values is larger, depending on the crystal orientation. A value for the maximum nonlinear coefficient, which is averaged over the possible individual crystal orientations, with equal statistical weight, can be calculated by

$$d_{\mathrm{m,ave}}^{\max} = \frac{\int_0^{2\pi}\int_0^{\pi} d_{\mathrm{m}}(\theta,\phi,0^\circ)\sin\phi\,\mathrm{d}\phi\,\mathrm{d}\theta}{4\pi} = 12.9\ \mathrm{pm/V} \quad (9)$$

when assuming the NLO coefficients of bulk crystals. This value holds only as an average of the maximum for a large number of individually measured crystal responses and has basically no meaning for a single crystal. These two benchmarks hold only if all three independent tensor elements stay constant for the nanocrystals.

To conclude, a variation in the minimum SH response is only due to size variation, while the maximum SH response varies with crystal size and orientation. The minimum therefore acts as a hard benchmark to test the SH response of the nanocrystals, while the maximum acts as a second benchmark, as long as the examined crystals as a whole are representative, i.e., the number of examined crystals is large. In the experiments the number of examined crystals within a batch ranges between 15 and 51, therefore we use both benchmarks for analysis. The exact experimental SH response values can now be compared to the theoretical values, using the calculated effective NLO coefficients, adding knowledge about crystal size, and employing Eq. (5).

Unfortunately, it is quite challenging to determine the size of individual nanocrystals *in situ*. One would have to do simultaneous examination by electron microscopical means and by NLO excitation. Especially at sizes below 20 nm, even scanning electron microscopes are unlikely to determine the crystal size with sufficient accuracy. A solution to this problem is to take into account the size distribution of the crystals, since the samples are not monodisperse, and to correlate this distribution with that of the SH signals.

3. Systematic losses

The effective nonlinear coefficients $d_{\mathrm{m}}(\theta,\phi,\psi)$ determine the total emitted power, but this will only be measurable when sampling all the emitted light, which is hardly possible. In a real setup, a systematic error in the estimation of the light radiated by the point dipole occurs: The light is detected from a solid angle smaller than the full sphere and can only be extrapolated to the total radiated light. This is not necessarily equal to the truly total radiated light, without knowledge about the spatial radiation pattern, especially because the crystal does not emit isotropically, since it lies directly on the dielectric surface of the glass substrate.

The dipole emission near planar interfaces is a well-known problem, first described by Sommerfeld for radiowaves and re-emerging in the field of nano-optics.[29] The far-field radiation patterns for a point dipole antenna for a 532-nm wavelength, 5 nm away from a glass substrate, for different dipole orientations have been calculated, using expressions of Novotny *et al.*[30] Figure 3 shows three examples, with the collection angle displayed as the shaded area and γ representing the angle of the dipole moment with respect to the surface. Integration over the collection angle, normalized to the total emission, gives the detected light fraction.

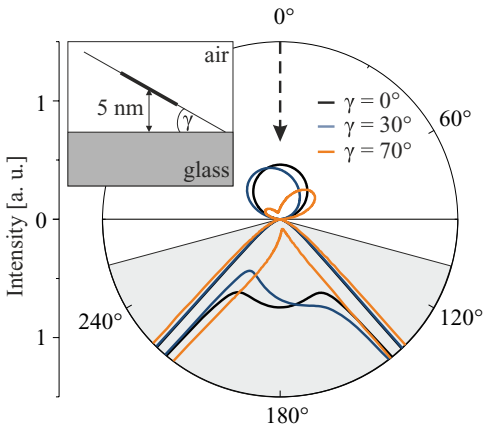

FIG. 3. (Color online) Angular dependent radiated intensity for point dipole antennas on a glass substrate, in the laboratory frame of reference. The pump light propagates parallel to the dashed arrow. The upper halfspace consists of air, the lower of glass, the shaded region marks the collection angle, γ represents the angle between antenna and surface.

With the nanocrystal so close to the substrate almost all radiated light is coupled in the substrate within the collection angle, and the collected light varies only slightly when the orientation of the dipole moment changes. With a 150° collection angle, which is achieved by the oil-immersion objective used, having a 1.45 NA, a collection efficiency of 0.81 ± 0.08 is achieved.

Overall the calculated error due to the incomplete collection and unknown dipole moment orientation is, on average, smaller than 10%. Since this error is small on average, it is assumed that 81% of the total emission is collected, to extrapolate the measured SH power, which removes the need for an orientation-dependent correction factor.

IV. ELECTRON MICROSCOPICAL CHARACTERIZATION

Transmission electron microscopy (TEM) with energy-dispersive x-ray spectroscopy (EDX) was performed on a Phillips CM30T. A Phillips CM300UT FEG was used for high-resolution imaging (HRTEM). The size and shape of the crystals were examined for all batches by TEM imaging. See Fig. 4(a) for an overview image for the AG batch. Using EDX, the Nb and O contents at several arbitrary positions of each batch were checked. The measurements show that Nb and O are spatially correlated in the crystals and occur at the expected concentration ratio, while other chemical contaminations, especially F and N from the neutralization or Y and Zr from the vials used in the separation procedure, are not detected. The full chemical composition of the crystals could not be determined, as the detection of Li is very challenging using EDX.

To verify the expected crystal structure of $LiNbO_3$, especially in etched batches, selective-area electron diffraction patterns of regions with many crystals were acquired, as shown, e.g., in Fig. 4(b). All the batches exhibit the Debye-Scherrer ring diffraction patterns expected for $LiNbO_3$. No additional

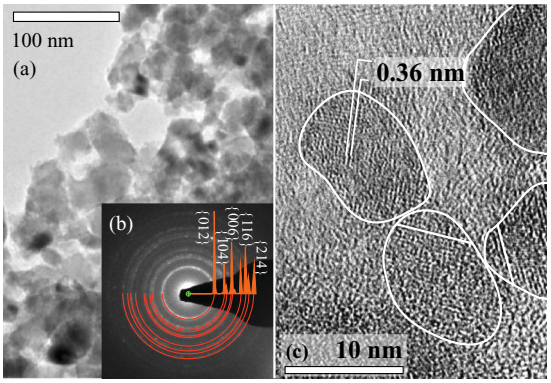

FIG. 4. (Color online) (a) TEM bright-field image of the AG batch. (b) Electron diffraction Debye-Scherrer pattern of crystals of M10. Reflection rings of $LiNbO_3$ (ICDS database No. 28294) are outlined and indexed, indicating phase-pure $LiNbO_3$. (c) High-resolution TEM image of H20. Crystal contours and some prominent lattice fringes are outlined in white.

Bragg peaks were detected, indicating the phase purity of the products. Furthermore, the nearly closed diffraction rings indicate that no preferred crystal orientation exists within the agglomerates, which is expected for soft agglomerates, i.e., loose clusters of particles.

For some selected etched batches HRTEM imaging was performed. A HRTEM image of batch H20 is shown in Fig. 4(c) where a number of individual $LiNbO_3$ nanocrystals can be identified due to their lattice fringe contrast. Visible lattice fringes in $LiNbO_3$ are predominantly the $\{012\}$ planes, since they exhibit the largest plane spacing with $d = 0.36$ nm.

For statistical analysis of crystal sizes determined by TEM, discernible crystal contours were approximated with ellipses. In all batches between 300 and 600 individual crystals were analyzed, and the individual axes and axis ratios were determined. Mean crystal diameters were calculated by averaging long and short axes of the contours. The crystal diameters were

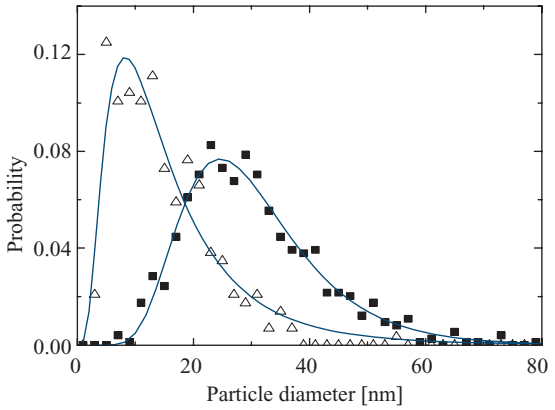

FIG. 5. (Color online) Crystal size distribution for two batches, with lognormal fits shown as lines. The crystal size was determined by averaging the long and short axes. Batches: filled squares represent AG, which peaks at 25 nm and averages to 30 nm. Open triangles represent M30, which peaks at 9 nm and averages to 13 nm. Data are normalized to a cumulated probability of 1, and the statistical bin size is 2 nm.

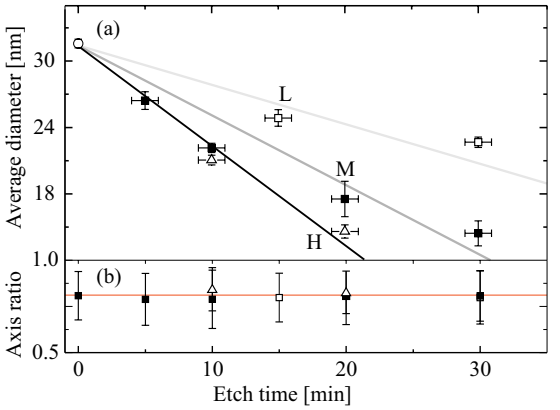

FIG. 6. (Color online) (a) Mean crystal diameter versus etching time for three HF concentrations: open squares, 95 mM HF; filled squares, 180 mM HF; and open triangles, 335 mM HF. The lines are linear fits to the data. (b) Averaged crystal axis ratios for different etching treatments. Symbols are the same as in (a), and bars indicate the standard deviations of the axis ratio. The horizontal (orange) line at an 0.8 axis ratio is a guide for the eye.

counted with bin sizes of 2 nm to get size distributions, which were approximated by lognormal distribution functions.

Identification of crystals smaller than 5 nm in agglomerates is a demanding task for TEM bright field imaging. If the size distributions in this size region are needed, the extrapolated value of the lognormal function is used.

Figure 5 shows the particle size distributions for batches AG and M30, with their respective lognormal fits. Due to the asymmetry of the distributions, the average crystal diameter is unlikely to be the same as the most frequent crystal diameter. This asymmetry is characterized by the skewness, by dividing the difference of the average and maximum values by the standard deviation. This skewness stays constant for all samples at 0.4 ± 0.15. Note that we refer to the probability of finding a single crystal at a certain size, which is the relative number density of particles, and not, e.g., to the relative material volume, as we later examine optically and count individual nanocrystals.

The average diameter development upon etching is shown in Fig. 6(a). It is clear that size reduction is faster at higher HF concentrations. The data suggest a linear diameter reduction over etch time in the examined size range of 30 nm and below. See Table III for the determined etch rates. A linear dependence on acid concentration, at the rate of 2.9 ± 0.7 pm min^{-1} mM^{-1}, is found.

The development of the axis ratios was also examined. Figure 6(b) shows the average axis ratios for all samples; the bars indicate the corresponding standard deviations. It is

TABLE III. Etch rates for HF concentrations used.

HF concentration (mM)	Etch rate (nm min^{-1})
95	0.36 ± 0.1
180	0.65 ± 0.1
335	0.90 ± 0.1

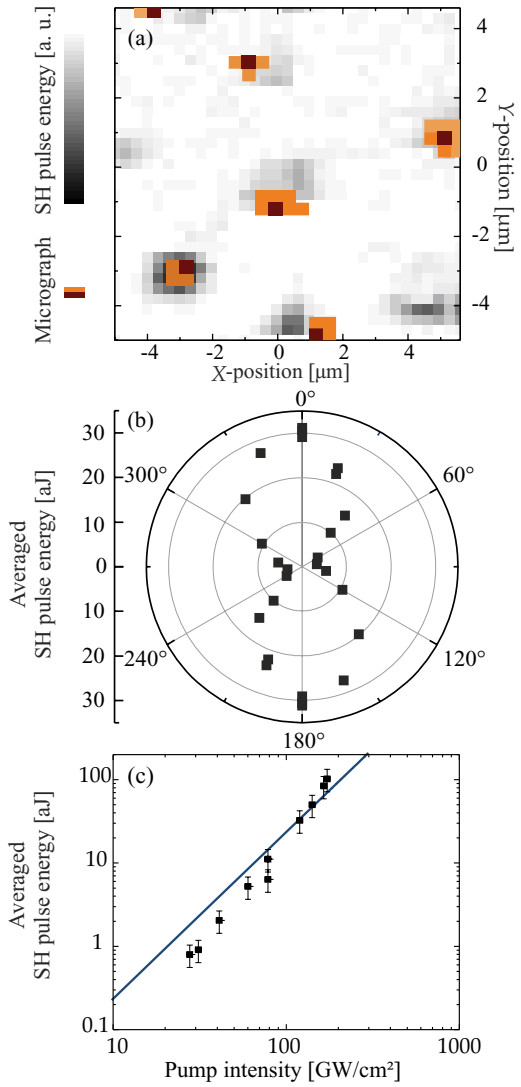

FIG. 7. (Color online) (a) Overlain light microscopical image, in red scale with greatly enhanced contrast, and scanned SH response, in gray scale, of a typical sample. (b) Averaged polarization-dependent SH pulse energy for a crystal from batch M10 at $I = 80$ GW/cm^2 pump intensity. (c) Averaged SH pulse energy versus pump intensity for an AG crystal with minimum-conversion light polarization direction. The solid line illustrates the predicted $\propto I_p^2$ curve with $d_m = 5.6$ pm/V and $r = 28$ nm.

noticeable that the ratios, as well as the standard deviations, remain constant at ≈0.8 and ≈0.15, respectively.

V. SECOND HARMONIC CHARACTERIZATION

The polarization-dependent frequency conversion of 15 single crystals from each of batches AG, M5, M10, and M20, as well as 51 crystals from M30, were studied for statistical analysis of the conversion behavior. In Fig. 7(a) an overlay of the microscopical image of a sample region and the corresponding scanned SH response is shown to illustrate the measurements. There is about one light scattering object per 10 μm^2. The light scattering of subresolution objects is correlated with the SH response, therefore the microscopical imaging is sufficient for a preliminary sample selection. Figure 7(b) shows a typical polarization-dependent SH response for an optical subresolution object of sample M10, which is identified to be a single particle. The predicted response with a maximum conversion, here at 0°, and a minimum conversion, perpendicular to that of the maximum, can be seen. In this case it is in average 31 and 3.4 aJ per pulse, respectively.

For some selected particles the dependence of the generated SH power on the pump intensity was also measured. Figure 7(c) shows the results of such a measurement on the logarithmic scale for a crystal of the AG sample in the minimum-conversion polarization orientation. This specific crystal was destroyed at $I \approx 200$ GW/cm^2. A power-law dependence is obvious. The determined exponents range from 2.05 to 2.6. Although they are systematically higher than that of the expected quadratic dependence, we cannot rule out experimental limitations that lead to a slight overestimation of the exponent, like a slightly sublinear detector response.

Most polarization-dependent SH responses of the crystals show the distinctive peanut-shaped polar plot, as in Fig. 7(b). These are the response measurements yielding the highest modulation between minimum and maximum response. Figure 8 shows the SH response of one of the crystals from batch M30, which has a low modulation, its polar axis is almost parallel to the beam direction. Here a polar behavior is seen along the vertical axis. Perpendicular to that, another bulge is seen. Only for this particular plot, the determination of the angles and scaling of the theoretical curve, which is shown by the thick (blue) line, was done by fitting. That fit yields the parameters $\theta = 65° \pm 5°$, $\phi = 75° \pm 5°$, and $L = 21 \pm 0.5$ nm.

As the measurement of the polarization-dependent SH response is done with several crystals from each of the M sets of batches and the reference, an average minimum and maximum of the SH pulse energy as a function of the average crystal diameter can be determined. This is done also for the calculated d_m^{min} and d_m^{max}. To clarify, there are three averages up to this point: For a single crystal, the response is averaged over several pulses. The maximum and minimum

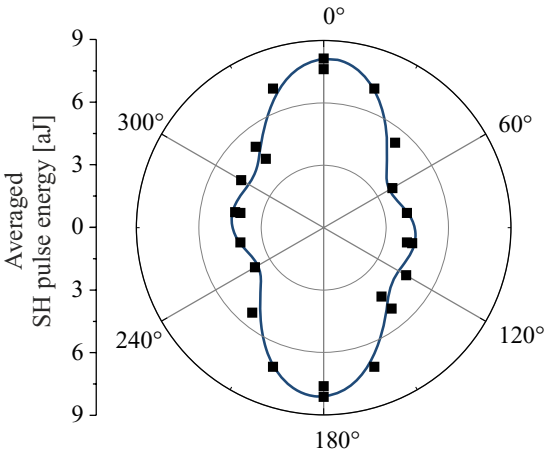

FIG. 8. (Color online) Polar plot of the averaged SH pulse energy of a crystal from batch M30. The thick (blue) line is a calculated prediction with $\theta = 65° \pm 5°$ and $\phi = 75° \pm 5°$. The prediction curve was scaled via the minimum SH response.

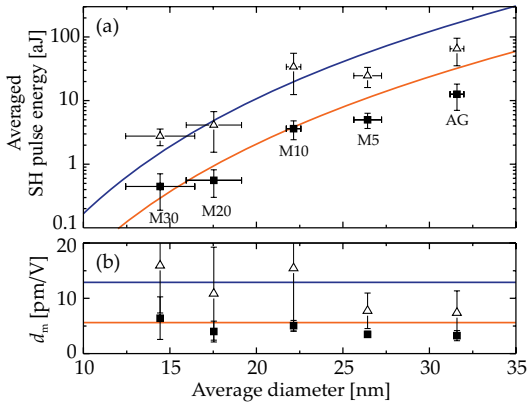

FIG. 9. (Color online) (a) Averaged SH pulse energy versus crystal size in a semilogarithmic plot. The minimum (filled squares) and maximum (open triangles) polarization-dependent values are shown. The upper (blue) line shows the prediction using a pump intensity of $I = 80$ GW/cm^2 and $d_m = 12.9$ pm/V; the lower (orange) line uses $d_m = 5.6$ pm/V. (b) Calculated d_m versus average crystal size; line colors and symbols as in (a).

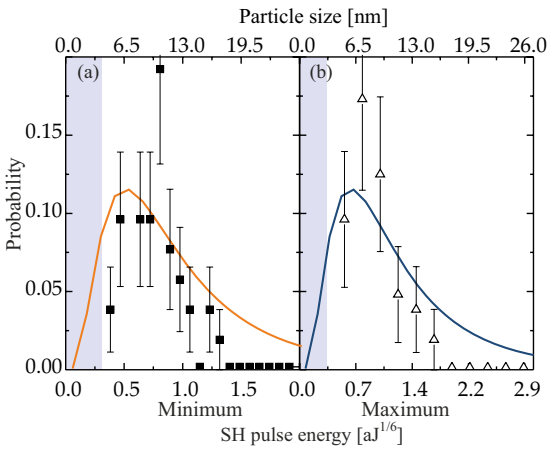

FIG. 10. (Color online) Occurrence probability of the sixth root of the SH pulse energy in M30: (a) At minimum conversion. The solid (orange) line was predicted using the measured crystal size distribution and $d_m^{min} = 5.6$ pm/V. (b) At maximum conversion. The solid (blue) line was predicted, using the measured crystal size distribution and $d_{m,ave}^{max} = 12.9$ pm/V. Filled squares and open triangles show the sixth roots of the respective measured SH pulse energies. The shaded region indicates where the crystal response is lower than the substrate response.

responses of crystals are averaged within a batch and used to calculate the NLO coefficients using the previously determined average crystal size. Figure 9(a) shows the results for the SH pulse energy, together with the curves predicted according to Eq. (5). Figure 9(b) shows the calculated d_m together with the mean d_m values predicted based on the d values of bulk crystals. The data are in good agreement with the predictions from our model. Averaging over all batches, the measured NL coefficients yield $d_m^{min} = 4.5 \pm 1.3$ pm/V and $d_{m,ave}^{max} = 11 \pm 7$ pm/V.

Since the averaged measured values are in good agreement with our model predictions, the individual responses of the crystals of batch M30 are examined. Crystals smaller than 10 nm are especially interesting, considering that there might be a critical size for maintaining inversion symmetry and second-order nonlinear response. So the batch with the smallest average crystal diameter is used for in-detail studies. For better statistical analysis, the number of examined crystals is increased to 51.

Since Eq. (5) shows that $P_2 \propto L^6$, the sixth root of the SH pulse energy is a length scale. Therefore, the sixth roots of minimum and maximum SH pulse energies for all 51 crystals were counted in bins with widths of 0.09 and $0.25\sqrt[6]{\text{aJ}}$, respectively. This gives us an SH response distribution, which can be compared to the crystal size distribution.

For this, the crystal size distribution of M30, determined by TEM examination, was converted into a $\sqrt[6]{W_2}$ scale using Eq. (5) and the predicted d_m^{min} and $d_{m,ave}^{max}$. Figure 10 shows the outcome for minimum and maximum conversion. The probability of the measured SH distribution, as well as the calculated SH distribution, is normalized to a cumulated probability of 1. Note that these diagrams involve no fitting.

Using a pump intensity of $I = 80$ GW/cm^2, a sample of the batches AG and M30 was examined for its long-term stability against illumination. The detected average SH light intensity changed by less than 15% for up to 3 h of illumination, indicating that exposure to pump light of this intensity has no effect on the crystals.

VI. DISCUSSION

A. Nanocrystal etching

The observed reduction in the average crystal size is linear over time for the three acid concentrations used. The axis ratio is constant for all batches, as is the spread of axis ratios. This behavior is quite peculiar, since the bulk material of $LiNbO_3$ shows strongly axis-dependent etch rates.[31,32] The differential etching of bulk material is so strong in $LiNbO_3$ that it is used to fabricate free-standing microstructures and nanostructured bulk crystals.[33,34] But the behavior of the crystal-axis ratios seen in our experiments with nanocrystals rules out differential etching: This would cause a change in the average axis ratios, if the long and short axes are in any way correlated with the crystal axes. If an axis correlation does not exist, differential etching would result mainly in a change in the standard deviations. In the experiments, however, we observe a constant value of the crystal axis ratios, being 0.8 ± 0.1 for the AG crystals as well as for the etched crystals. So the dissolution by HF seems to have no impact on the nearly spherical form of the nanocrystals.

For bulk material the differential etch rates are known: The $+c$ crystal face shows no etching, the $-c$ face etches at a rate of 1.7 nm/min with 10% HF, and the a and b faces etch very slowly, at etch rates about 10 times lower than that of the $-c$ face.[31] A quadratic concentration dependence of between 10% and 48% for all nonzero etch rates has been measured. Extrapolating this to the concentration we used yields an etch rate of 0.5 ± 0.2 nm/min for the $-c$ face for 5% HF, while we measured a 0.65 ± 0.1 nm/min diameter reduction. So the etch rate of the quasi-isotropic etching of the nanocrystals is consistent with the etch rate of the $-c$ face of bulk crystals. Probably the crystals etch from the $-c$ face, but the conservation of the spherical shape indicates a similar etch rate for the a and b faces at these small crystal sizes.

A possible explanation for the quite different behavior of the nanocrystals in comparison to that of the bulk material is that the chemical etching cannot supply enough energy to the already large surface energy of the nanocrystals to generate morphologies other than almost spherical. Considering this, the $-c$ face etching determines the etch rate, but the crystals are unlikely to develop into small disks.

B. Nonlinear optical properties

$LiNbO_3$ nanocrystals of all sizes studied in this work have shown an unambiguous NLO response. Hence, as the main outcome of our work, there are no indications of a size-induced symmetry change, at least for particle diameters down to 5 nm. In detail, the experimental data for maximal and minimal conversion show a good agreement with the calculations for average particle sizes between 14 and 32 nm, as shown in Fig. 9. The predicted effective NLO coefficients from the model are $d_{\mathrm{m}}^{\mathrm{min}} = 5.6$ pm/V and $d_{\mathrm{m,ave}}^{\mathrm{max}} = 12.9$ pm/V. They agree with the measured values $d_{\mathrm{m}}^{\mathrm{min}} = 4.5 \pm 1.3$ pm/V and $d_{\mathrm{m,ave}}^{\mathrm{max}} = 11 \pm 7$ pm/V: The bulk crystal NLO coefficients remain unchanged. The relative errors for maximal conversion are larger than the errors for minimal conversion, since it has more statistical variation of results and a broader SH energy distribution, while at minimal conversion the distribution is only due to size variation within the sample.

Most crystals exhibit a polar-axis-determined peanut shape of the polarization-dependent SH response in the polar plot, like the one shown in Fig. 7(b). This is expected for a crystal that has its c axis oriented in such a way that the polar axis has a significant component parallel to the substrate. Here the impact of the polar axis of the crystal prevails, i.e., the components d_{33} and d_{31} could be used for a description of the data. According to the model, these are all orientations with roughly $0 < \phi < 70^\circ$ or $110^\circ < \phi < 180^\circ$, which would constitute most of the crystals. To show the influence of the third component d_{22} directly, one needs a crystal that has the c axis almost perpendicular to the substrate, within the afore-mentioned 40° window. Such a crystal produces a response like the one shown in Fig. 8. The additional bulge perpendicular to the primary polar axis can only be described when d_{22} is included. This is an experimental confirmation that the nanocrystals have the point group $3m$, via NLO means. The nanocrystals belong to the same point group as the ferroelectric $LiNbO_3$ bulk crystals. In this case the point group $3m$ means that the nanocrystals are at least pyroelectric and spontaneously polarized. We cannot determine, with our optical method, whether the direction of this spontaneous polarization can be switched by electrical fields. This is a further requirement for a crystal to be called ferroelectric.

A closer look at Fig. 10 reveals that, also for smaller crystals, about 5 to 10 nm in diameter, there is agreement between theory and data, i.e., the particles still show the full NLO response. So we can rule out centrosymmetric $LiNbO_3$ crystals larger than 5 nm. The light conversion and noncentrosymmetry of even smaller crystals, in the 3- to 5-nm range, is difficult to ascertain, as the detection threshold defined by the substrate response skews the statistics. In contrast to a sudden size-induced loss of noncentrosymmetry, there are also theoretical approaches that predict a more gradual decrease: *Ab initio* calculations show[35] that the surface termination changes the crystal composition with respect to that of the bulk material, which could result in centrosymmetry. We cannot determine whether or not this layer exists, but it has to be thinner than about 1 nm.

VII. SUMMARY

Wet chemical etching of sol-gel synthesized crystals, using HF, successfully produces $LiNbO_3$ nanocrystals in size ranges from 50 down to 5 nm, with a nearly spherical morphology. These particles show SH generation, in good agreement with the predictions from a straightforward model, which treats the nanocrystals as emitting point dipoles, whereas the determining coefficients are those of the bulk material. This indicates that the NLO coefficients known from the bulk material remain valid also for such small nanocrystals: The nanocrystals still have the same crystal structure as the bulk material.

ACKNOWLEDGMENTS

Helpful discussions with Boris Sturman and Frank Kühnemann are greatly appreciated. Financial support from the DFG (NSF/DFG Grant No. BU 913/21) and the Baden-Württemberg Stiftung (KFN IV/D2) is gratefully acknowledged.

*Corresponding author: Bastian.Knabe@ipm.fraunhofer.de

[1] K. Binder, Ferroelectrics **73**, 43 (1987).
[2] J. Junquera and P. Ghosez, Nature **422**, 506 (2003).
[3] K. Ishikawa, K. Yoshikawa, and N. Okada, Phys. Rev. B **37**, 5852 (1988).
[4] K. Uchino, E. Sadanaga, and T. Hirose, J. Am. Ceram. Soc. **72**, 1555 (1989).
[5] A. Rudiger, T. Schneller, A. Roelofs, and S. Tiedke, Appl. Phys. A **80**, 1247 (2005).
[6] M. Yashima, T. Hoshina, D. Ishimura, S. Kobayashi, and W. Nakamura, J. Appl. Phys. **98**, 014313 (2005).
[7] L. Curecheriu, M. T. Buscaglia, V. Buscaglia, Z. Zhao, and L. Mitoseriu, Appl. Phys. Lett. **97**, 242909 (2010).
[8] S. A. Basun, G. Cook, V. Y. Reshetnyak, A. V. Glushchenko, and D. R. Evans, Phys. Rev. B **84**, 024105 (2011).
[9] A. N. Morozovska, E. A. Eliseev, G. S. Svechnikov, and S. V. Kalinin, J. Appl. Phys. **108**, 042009 (2010).
[10] B. Knabe, D. Schütze, T. Jungk, M. Svete, W. Assenmacher, W. Mader, and K. Buse, Phys. Stat. Sol. A **208**, 857 (2011).
[11] F. Johann, T. Jungk, S. Lisinski, A. Hoffmann, L. Ratke, and E. Soergel, Appl. Phys. Lett. **95**, 202901 (2009).
[12] L. Arizmendi, Phys. Stat. Sol. **201**, 253 (2004).

[13]L. Bonacina, Y. Mugnier, F. Courvoisier, R. Le Dantec, J. Extermann, Y. Lambert, V. Boutou, C. Galez, and J. P. Wolf, Appl. Phys. B **87**, 399 (2007).
[14]M. Zielinski, D. Oron, D. Chauvat, and J. Zyss, Small **5**, 2835 (2009).
[15]S. Tripathi, B. J. Davis, K. C. Toussaint, and P. S. Carney, J. Phys. B **44**, 015401 (2011).
[16]Y. Nakayama, P. J. Pauzauskie, A. Radenovic, R. M. Onorato, R. J. Saykally, J. Liphardt, and P. Yang, Nature **447**, 1098 (2007).
[17]L. Le Xuan, S. Brasselet, F. Treussart, J. F. Roch, F. Marquier, D. Chauvat, S. Perruchas, C. Tard, and T. Gacoin, Appl. Phys. Lett. **89**, 121118 (2006).
[18]C.-L. Hsieh, R. Grange, Y. Pu, and D. Psaltis, Opt. Express **17**, 2880 (2009).
[19]E. Sliwinska, S. Mansurova, U. Hartwig, K. Buse, and K. Meerholz, Appl. Phys. B **95**, 519 (2009).
[20]E. Delahaye, N. Tancrez, T. Yi, I. Ledoux, J. Zyss, S. Brasselet, and R. Clement, Chem. Phys. Lett. **429**, 533 (2006).
[21]M. J. Pooley and A. V. Chadwick, Radiat. Eff. Defect. Sol. **158**, 197 (2003).
[22]See Supplemental Material at http://link.aps.org/supplemental/10.1103/PhysRevB.86.195428 for the complete description of the etching procedure and the procedure to ensure that only single crystals are present in the center of the pump focus.
[23]D. Schütze, B. Knabe, M. Ackermann, and K. Buse, Appl. Phys. Lett. **97**, 242908 (2010).
[24]C. F. Bohren and D. Huffman, *Absorption and Scattering of Light by Small Particles* (John Wiley and Sons, New York, 1983).
[25]D. E. Zelmon, D. L. Small, and D. Jundt, J. Opt. Soc. Am. B **14**, 3319 (1997).
[26]A. Yariv, *Optical Waves in Crystals* (John Wiley and Sons, New York, 1988).
[27]J. D. Jackson, *Classical electrodynamics* (John Wiley and Sons, New York, 1998).
[28]C.-L. Hsieh, Y. Pu, R. Grange, and D. Psaltis, Opt. Express **18**, 11917 (2010).
[29]A. Sommerfeld, Ann. Phys. **28**, 665 (1909).
[30]L. Novotny and B. Hecht, *Principles of Nano-Optics* (Cambridge University Press, Cambridge, 2006).
[31]C. L. Sones, S. Mailis, W. S. Brocklesby, R. W. Eason, and J. R. Owen, J. Mater. Chem. **12**, 295 (2002).
[32]A. B. Randles, M. Esashi, and S. Tanaka, IEEE T. Ultrason. Ferr. **57**, 2372 (2010).
[33]C. Y. J. Ying, C. L. Sones, A. C. Peacock, F. Johann, E. Soergel, R. W. Eason, M. N. Zervas, and S. Mailis, Opt. Express **18**, 11508 (2010).
[34]A. Ofan, M. Lilienblum, O. Gaathon, A. Sehrbrock, A. Hoffmann, S. Bakhru, H. Bakhru, S. Irsen, R. M. Osgood, and E. Soergel, Nanotechnology **22**, 285309 (2011).
[35]S. Sanna and W. G. Schmidt, Phys. Rev. B **81**, 214116 (2010).